# Earth's Future

**Corresponding author:**
M. J. Mills, mmills@ucar.edu

# Multidecadal global cooling and unprecedented ozone loss following a regional nuclear conflict

Michael J. Mills[1], Owen B. Toon[2], Julia Lee-Taylor[1], and Alan Robock[3]

[1]NCAR Earth System Laboratory, Boulder, Colorado, USA, [2]Laboratory for Atmospheric and Space Physics and Department of Atmospheric and Oceanic Sciences, University of Colorado Boulder, Boulder, Colorado, USA, [3]Department of Environmental Sciences, Rutgers, State University of New Jersey, New Brunswick, New Jersey, USA

**Abstract** We present the first study of the global impacts of a regional nuclear war with an Earth system model including atmospheric chemistry, ocean dynamics, and interactive sea ice and land components. A limited, regional nuclear war between India and Pakistan in which each side detonates 50 15 kt weapons could produce about 5 Tg of black carbon (BC). This would self-loft to the stratosphere, where it would spread globally, producing a sudden drop in surface temperatures and intense heating of the stratosphere. Using the Community Earth System Model with the Whole Atmosphere Community Climate Model, we calculate an *e*-folding time of 8.7 years for stratospheric BC compared to 4–6.5 years for previous studies. Our calculations show that global ozone losses of 20%–50% over populated areas, levels unprecedented in human history, would accompany the coldest average surface temperatures in the last 1000 years. We calculate summer enhancements in UV indices of 30%–80% over midlatitudes, suggesting widespread damage to human health, agriculture, and terrestrial and aquatic ecosystems. Killing frosts would reduce growing seasons by 10–40 days per year for 5 years. Surface temperatures would be reduced for more than 25 years due to thermal inertia and albedo effects in the ocean and expanded sea ice. The combined cooling and enhanced UV would put significant pressures on global food supplies and could trigger a global nuclear famine. Knowledge of the impacts of 100 small nuclear weapons should motivate the elimination of more than 17,000 nuclear weapons that exist today.

## 1. Introduction

In the 1980s, studies of the aftermath of a global nuclear conflict between the United States and the Soviet Union predicted that airborne particles, such as fine soil and smoke resulting from explosions and fires, could circle the globe, producing "twilight at noon," and cooling the surface for years, in what became known as "nuclear winter" [*Crutzen and Birks*, 1982; *Turco et al.*, 1983; *Pittock et al.*, 1985]. Further studies looked at perturbations to atmospheric chemistry, predicting that odd nitrogen produced by the largest nuclear weapons could loft to the stratosphere, resulting in significant ozone loss, and an "ultraviolet spring" to follow [*National Research Council*, 1985; *Stephens and Birks*, 1985]. Leaders in the United States and the Soviet Union became aware of the global environmental damage of nuclear war and subsequently negotiated treaties that have significantly reduced their nuclear stockpiles from their peak near 65,000 in 1986 to less than 20,000, a decline that continues with further negotiations in recent years [*Robock et al.*, 2007a; *Toon et al.*, 2007, 2008]. Nevertheless, significant numbers of weapons remain, and the number of nuclear-armed states continues to increase.

Since 2007, studies have revisited the issue of global nuclear conflicts with modern global climate models, confirming the severity of the climatic impacts that had been predicted with simple climate models or with short simulations of low-resolution atmospheric general circulation models in the 1980s [*Robock et al.*, 2007a], and raising new concerns about severe global climatic impacts of regional nuclear conflicts [*Robock et al.*, 2007b; *Toon et al.*, 2007; *Mills et al.*, 2008; *Stenke et al.*, 2013]. Even the smallest of nuclear weapons, such as the ~15 kt weapon used on Hiroshima, exploding in modern megacities would produce firestorms that would build for hours, consuming buildings, vegetation, roads, fuel depots, and other infrastructure, releasing energy many times that of the weapon's yield [*Toon et al.*, 2007]. *Toon et al.* [2007] estimated the potential damage and smoke production from a variety of nuclear exchange scenarios, and found that smoke would initially rise to the upper troposphere due to pyroconvection. *Robock et al.* [2007b] examined the climatic impact of the smoke produced by a regional conflict in the subtropics in

which two countries each used 50 Hiroshima-size (15 kt) nuclear weapons, creating such urban firestorms. Using the global climate model GISS ModelE (Goddard Institute for Space Studies, New York), they calculated that nearly all the 5 Tg of smoke produced would rise to the stratosphere, where it would spread globally, reducing the global average temperature by 1.25°C for 3–4 years and by more than 0.5°C for a decade. This effect was longer lasting than that found in previous "nuclear winter" studies, because older models could not represent the rise of smoke into the stratosphere. *Mills et al*. [2008] then used a chemistry-climate model to calculate that the concurrent heating of the stratosphere by up to 100°C would produce global ozone loss on a scale unprecedented in human history, lasting for up to a decade.

Recently, *Stenke et al*. [2013] used a third independent model to confirm the major findings of these two previous studies. That study used the chemistry-climate model SOCOL3 to assess impacts on climate and stratospheric ozone for a range of inputs and particle sizes. The study coupled a mixed-layer ocean with a depth of 50 m and a thermodynamic sea ice module to a high-top atmospheric model, which calculated chemistry effects in agreement with *Mills et al*. [2008]. Unlike *Robock et al*. [2007b], the study did not consider active ocean dynamics, and hence could not incorporate the climate effects of changing ocean circulation. The inclusion of only the top 50 m of ocean limits the thermal inertia effects that occur in the presence of a deep ocean, making surface temperature responses too rapid, as the heat content of the deeper ocean is not considered.

Here we present the first study of this scenario with an Earth system model, coupling a chemistry-climate model to interactive ocean, sea ice, and land components.

## 2. Model Description

### 2.1. CESM1(WACCM)

We revisit the scenario of nuclear war between India and Pakistan, each side using 50 Hiroshima-size weapons in megacities on the subcontinent, using the first version of NCAR's Community Earth System Model (CESM1), a state-of-the-art, fully coupled, global climate model, configured with fully interactive ocean, land, sea ice, and atmospheric components [*Hurrell et al*., 2013]. For the atmospheric component, we use the Whole Atmosphere Community Climate Model, version 4 (WACCM4), which is a superset of version 4 of the Community Atmospheric Model (CAM4), and includes all the physical parameterizations of that model [*Neale et al*., 2013]. WACCM is a "high-top" chemistry-climate model that extends from the surface to $5.1 \times 10^{-6}$ hPa (~140 km). It has 66 vertical levels and horizontal resolution of 1.9° latitude $\times$ 2.5° longitude. WACCM includes interactive chemistry that is fully integrated into the model's dynamics and physics. Heating the stratosphere, for example, feeds back onto chemical reaction rates. Photolysis rates are calculated based on extinction of exoatmospheric flux from overhead ozone and molecular oxygen, and are unaffected by aerosol extinction. WACCM uses a chemistry module based on version 3 of the Model for Ozone and Related Chemical Tracers (MOZART) [*Kinnison et al*., 2007], tailored to the middle and upper atmosphere. The chemical scheme includes 59 species contained in the $O_x$, $NO_x$, $HO_x$, $ClO_x$, and $BrO_x$ chemical families, along with $CH_4$ and its degradation products; 217 gas-phase chemical reactions; and heterogeneous chemistry that can lead to the development of the ozone hole. For our simulations, CESM1 includes the active land, ocean, and sea ice components described by *Lawrence et al*. [2011], *Danabasoglu et al*. [2012], and *Holland et al*. [2012], respectively. The full ocean model extends up to 5500 m in depth, and includes interactive, prognostic ocean circulation. The nominal latitude-longitude resolution of the ocean and sea ice components is 1°, the same as in CESM1(WACCM) simulations conducted as part of phase 5 of the Coupled Model Intercomparison Project [*Marsh et al*., 2013].

### 2.2. CARMA

We have coupled WACCM with version 3 of the Community Aerosol and Radiation Model for Atmospheres (CARMA3), a flexible three-dimensional bin microphysics package that we have adapted for the treatment of black carbon (BC) aerosol. This allows the BC to experience gravitational settling, and obviates the implementation of molecular diffusion, which the gas-phase tracers in WACCM experience at high altitudes. CARMA originated from a one-dimensional stratospheric aerosol code developed by *Turco et al*. [1979] and *Toon et al*. [1979] that included both gas-phase sulfur chemistry and aerosol microphysics. The model was improved and extended to three dimensions as described by *Toon et al*. [1988]. Extensive updates of the numerics continue to be made. For this study, we limit BC to one size bin of fixed radius.

As described below, we performed an ensemble of runs assuming a microphysical radius of 50 nm, to be consistent with the optical properties of BC assumed in the model's radiative code, which are derived from the Optical Properties of Aerosols and Clouds (OPAC) software package [*Hess et al.*, 1998]. Our previous studies of BC in the stratosphere from nuclear war and space tourism used these same optical properties, but with a radius for sedimentation that was twice as large [*Mills et al.*, 2008; *Ross et al.*, 2010]. We also conducted one perturbation run using the same 100 nm radius for sedimentation as those previous studies, for comparison in the coupled model.

We do not allow calculated particle populations to change radiatively or microphysically other than by rainout, sedimentation, and transport. The particles are assumed to be completely hydrophilic from the start, and hence are subject to rainout in the troposphere. We assume a mass density of $1 \, g \, cm^{-3}$ for each BC particle, consistent with measurements of atmospheric BC particles collected on filters, which are composed of smaller, denser particles aggregated in fractal formations with spatial gaps [*Hess et al.*, 1998]. As *Toon et al.* [2007] point out, coagulation of BC is likely to form chains or sheets, which would have the same or higher mass absorption coefficients as smaller BC particles. Drag forces would decrease sedimentation of such chains or sheets compared with aerosols that grow as simple spheres. Our neglect of coagulation, assuming a monodisperse distribution of 50 nm radius spheres, should more accurately predict stratospheric lifetime under conditions with fractals than a treatment of growth into larger spheres with faster sedimentation. *Toon et al.* [2007] also indicate that the BC is likely to become coated with sulfates, organics, and other nonabsorbing materials, which could act as lenses, refracting light onto the BC. This effect might increase absorption by ∼50%, leading to potentially greater impacts than those we modeled.

### 2.3. Model Setup

We have performed an ensemble of three "experiment" runs initialized with 5 Tg of BC with 50 nm radius over the Indian subcontinent. A fourth experiment run includes the same mass and spatial distribution of BC, with 100 nm sedimentation radius. We compare these experiment runs to an ensemble of three "control" runs without this additional BC. Each of these seven runs simulated the time period from 1 January 2013 to 1 January 2039, with concentrations of greenhouse gases and other transient constituents changing with time according to the specifications of the "medium-low emissions" Representative Concentration Pathway (RCP4.5) scenario [*Meinshausen et al.*, 2011], a baseline for climate projections. We also tried starting the simulated conflict on 15 May, as was done by *Robock et al.* [2007b] and *Stenke et al.* [2013], and found that the different season did not significantly affect the stratospheric distribution or climatic impact of the BC. Because of the prolonged surface cooling that we calculated, we extended our runs beyond the 10 year span used in previous studies to 26 years.

In the experiment runs, 5 Tg of BC was added to the initial atmospheric condition in a constant mass mixing ratio of $1.38 \times 10^{-6}$ kg/kg air between 300 and 150 hPa in a horizontal region spanning 50 adjacent model columns roughly covering India and Pakistan. The BC heats the atmosphere to extreme conditions, requiring a reduction of the model's standard time step from 30 to 10 min. Because this reduction in time step produces a significant increase in cloudiness in the model due to dependencies in the cloud parameterization, we reduced the time step consistently in the experiment and control runs. We also tried an alternate approach of increasing the dynamical substepping in the model, but found that the 16-fold increase in the number of substeps required to produce a stable result produced a similar increase in clouds to our original approach. We diagnose the effects of reducing the model time step in section 2.4.

The three members of each ensemble were configured with different initial conditions for the ocean, land, and sea ice components, derived from the ensemble of three RCP4.5 CESM1(WACCM) runs conducted as part of CMIP5 [*Marsh et al.*, 2013]. These components interact with the atmosphere, producing a representation of natural climate variability among the three runs in each ensemble. As we will show, the variability that we calculate within each ensemble is small compared to the differences between the experiment and control ensemble averages, indicating that the effects we calculate are not attributable to model internal variability.

### 2.4. Model Validation

To understand the effects of changing the model time step on our conclusions, we diagnosed the climate of one of our control runs for years 2023–2038, 16 years starting 10 years after the change in time

step, with reference to the climate of the same years from one of the CESM1(WACCM) CMIP5 runs for RCP4.5, the same forcing scenario used in our runs. The effect of increased low clouds is to change the global shortwave (SW) cloud forcing from −55 to −62 W m$^{-2}$. Observations from Clouds and Earth's Radiant Energy Systems (CERES) Energy Balanced and Filled (EBAF) put this forcing near −51 W m$^{-2}$, so the change produces a more reflective planet than is observed (A. Gettelman, personal communication). This may lead to an underestimation of the surface cooling anomaly in our calculations, because the effect of extinction in the stratosphere would be reduced if less SW radiation reaches the surface in both our control and experiment runs. At the same time, global longwave cloud forcing increases from 30 W m$^{-2}$ in our CMIP5 run to 34 W m$^{-2}$. Observations from CERES EBAF put this forcing near 26–27 W m$^{-2}$, so the change is toward more greenhouse warming from high clouds than is observed. This 4 W m$^{-2}$ increase in cloud forcing partially offsets the surface cooling effects of the 7 W m$^{-2}$ decrease in the SW. The changes in cloud forcing occur mostly in the tropics.

Because we started from an RCP4.5 scenario in 2013, the initial atmosphere is not in radiative balance, but is warming in response to anthropogenic greenhouse gases. The radiative imbalance at the top of the model is 0.977 W m$^{-2}$ in our CMIP5 run for years 2023–2038. The effect of increased clouds is to reduce this by a factor of 10 to 0.092 W m$^{-2}$, bringing the model close to the radiative balance that would be seen in a steady state, such as the static conditions used for previous nuclear winter calculations. We ran an additional case in which the 5 Tg of BC is added in year 10 of the control run. These calculations confirm that our calculated BC mass, and surface anomalies in SW flux, temperature, and precipitation are not significantly affected by any transient adjustments after the initial change in time step.

We also diagnosed effects on stratospheric chemistry by comparing the ensemble average column ozone from our control runs to the ensemble average from the CESM1(WACCM) CMIP5 runs for the first 6 years after we introduced the change in time step. We found no significant differences in either the global mean or latitudinal distribution of column ozone due to the change in time step. The effects of changing the model time step are relatively minor compared to those of 5 Tg of BC in the stratosphere, which is the focus of our study.

## 3. Results

### 3.1. BC Rise and Meridional Transport

As in previous studies of this scenario [*Robock et al*., 2007b; *Mills et al*., 2008], the BC aerosol absorbs SW radiation, heating the ambient air, inducing a self-lofting that carries most of the BC well above the tropopause. CESM1(WACCM) has 66 vertical layers and a model top of ∼145 km, compared to 23 layers up to ∼80 km for the GISS ModelE used by *Robock et al*. [2007b] and 39 layers up to ∼80 km for SOCOL3 used by *Stenke et al*. [2013]. As Figure 1 shows, we calculate significantly higher lofting than *Robock et al*. [2007b, compare to their Figure 1b], penetrating significantly into the mesosphere, with peak mass mixing ratios reaching the stratopause (50–60 km) within 1 month and persisting throughout the first year. This higher lofting, in conjunction with effects on the circulation we discuss later, produces significantly longer residence times for the BC than those in previous studies. At the end of 10 years, our calculated visible-band optical depths from the BC persist at 0.02–0.03, as shown in Figure 2. In contrast, Robock *et al*. [2007b] calculate optical depths near 0.01 only at high latitudes after 10 years, a level that our calculations do not reach for 15 years.

### 3.2. BC Burden, Rainout, and Lifetime

During the first 4 months, 1.2–1.6 of the 5 Tg of BC is lost in our 50 nm experiment ensemble, and 1.6 Tg in our 100 nm experiment, mostly due to rainout in the first few weeks as the plume initially rises through the troposphere (Figure 3a). This is larger than the 1.0 Tg initially lost in the study of *Mills et al*. [2008], which used a previous version of WACCM. This is likely due to the difference in our initial distribution of BC compared to that previous study, which injected 5 Tg into a single column at a resolution four times as coarse as ours. The more concentrated BC in the previous study likely produced faster heating and rise into the stratosphere, mitigating rainout. Our calculated rainout contrasts with the lack of significant rainout calculated by the GISS ModelE [*Robock et al*., 2007b], which assumes that BC is initially hydrophobic and becomes hydrophilic with a 24 h *e*-folding time scale. The mass burden reaching the stratosphere and impacts on global climate and chemistry in our calculations would doubtless be greater had we made
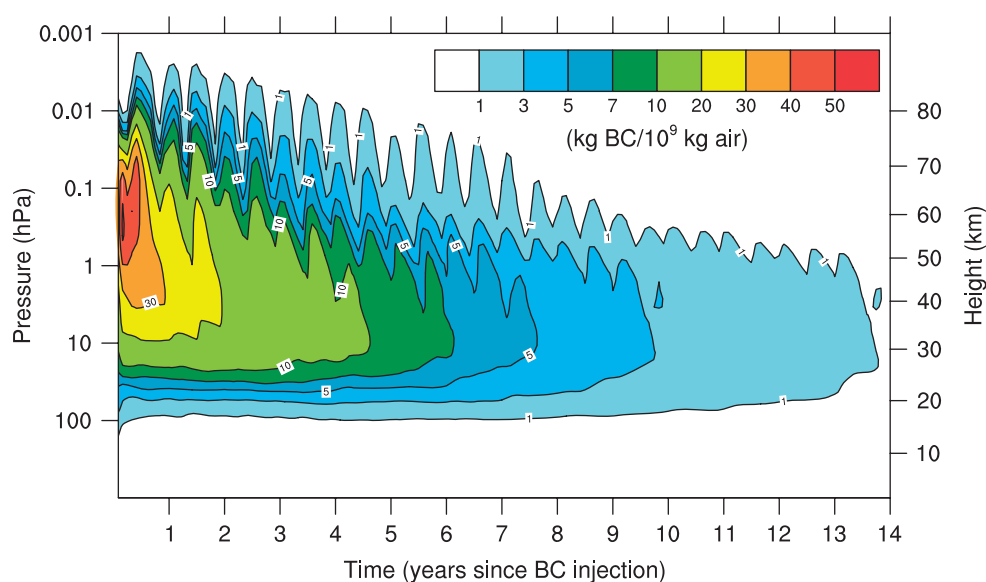
**Figure 1.** The time evolution of BC mass mixing ratio (kg BC/$10^9$ kg air) is shown for the average of the 50 nm experiment ensemble. The horizontal axis shows time in years since the emission of 5 Tg BC at 150–300 hPa on 1 January.
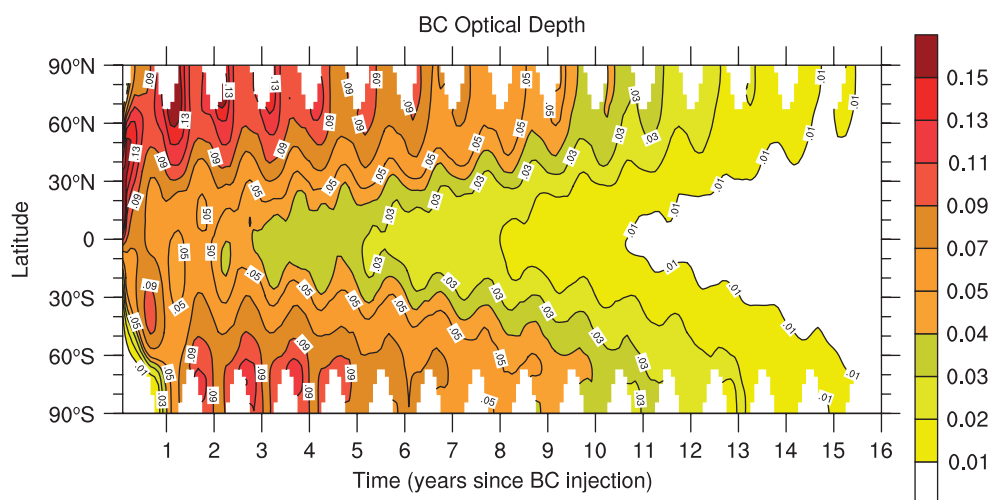


**Figure 2.** The time evolution of zonal mean total column BC optical depth in the visible part of the spectrum is shown for the 50 nm experiment ensemble average. The vertical axis shows latitude. The horizontal average shows time in years.

a similar assumption to the GISS ModelE. *Stenke et al.* [2013] calculate an initial rainout of ~2 Tg in their interactive 5 Tg simulations, which assumed BC radii of 50 and 100 nm in two separate runs. After initial rainout, the mass *e*-folding time for our remaining BC is 8.7 years for the average of our 50 nm experiment ensemble and 8.4 years for our 100 nm experiment, compared to the 6 years reported by *Robock et al.* [2007b], ~6.5 years by *Mills et al.* [2008], 4–4.6 years reported by *Stenke et al.* [2013], and 1 year for stratospheric sulfate aerosol from typical volcanic eruptions [*Oman et al.*, 2006]. Due to this longer lifetime, after about 4.8 years the global mass burden of BC we calculate in our ensemble is larger than that calculated by the GISS ModelE, despite the initial 28% rainout loss. After 10 years, we calculate that 1.1 Tg of BC remains in the atmosphere in our 50 nm experiment ensemble and 0.82 Tg in our 100 nm experiment, compared to 0.54 Tg calculated by the GISS ModelE and 0.07–0.14 Tg calculated by SOCOL3.

The long lifetime that we calculate results from both the very high initial lofting of BC to altitudes, where removal from the stratosphere is slow, and the subsequent slowing down of the stratospheric residual circulation. The Brewer-Dobson circulation is driven waves whose propagation is filtered by zonal winds,
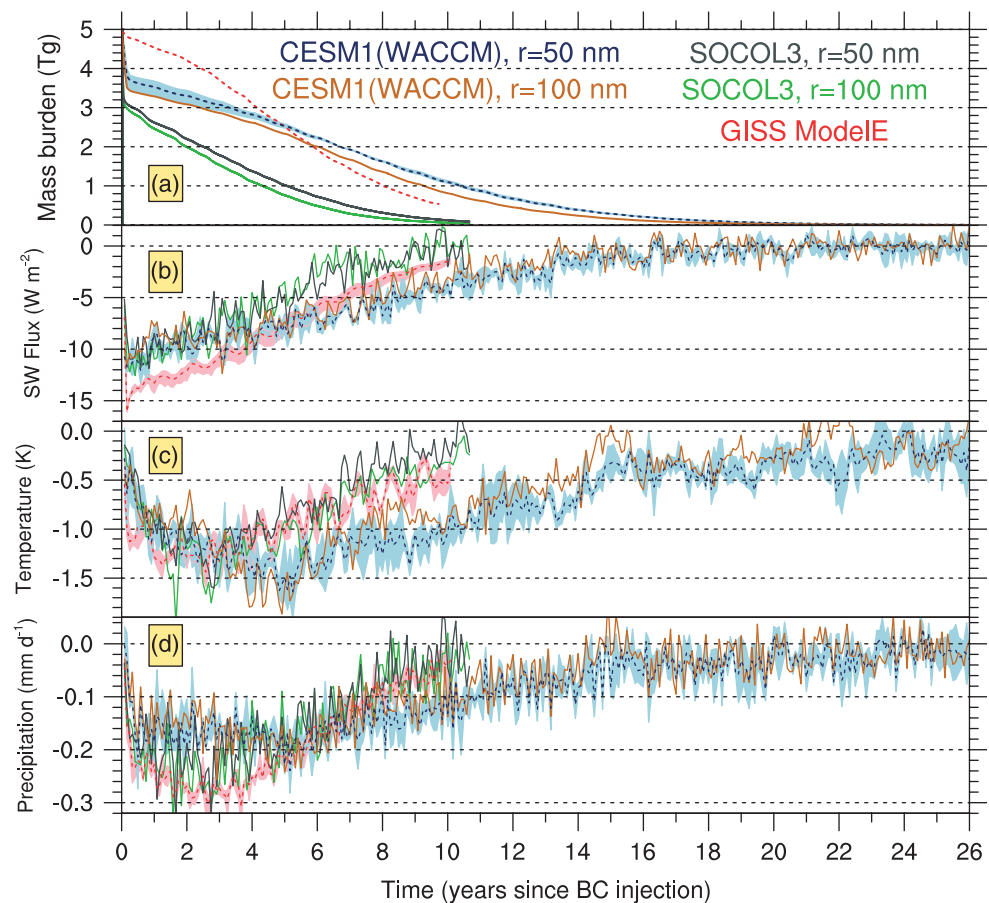
**Figure 3.** The monthly global mean time evolution is shown for (a) the mass burden of black carbon (Tg), (b) the shortwave net flux anomaly at the surface (W m$^{-2}$), (c) the surface temperature anomaly (K), and (d) the precipitation anomaly (mm/day). The dark blue dashed line and light blue shading show the average and range of our 50 nm experiment ensemble. The gold line shows our simulation assuming a 100 nm aerosol radius. The dark red dashed line and pink shading show the ensemble average and range for *Robock et al.* [2007a, 2007b] (data courtesy L. Oman). The grey and green lines show results from two 5 Tg BC simulations from *Stenke et al.* [2013] (data courtesy A. Stenke), with assumed aerosol radii of 50 and 100 nm, respectively. Ensemble anomalies are calculated with respect to the mean of the respective control simulation ensembles. Time 0 corresponds to the date of the BC injection (1 January in this study and 15 May in the other studies).

which are modulated by temperature gradients [*Garcia and Randel*, 2008]. As explained by *Mills et al.* [2008], the BC both heats the stratosphere and cools the surface, reducing the strength of the strato-spheric overturning circulation. Figure 4 shows the vertical winds in the lower stratosphere, which bring new air up from the troposphere and drive the poleward circulation, for the control and BC runs. The middle-atmosphere heating and surface cooling reduce the average velocity of tropical updrafts by more than 50%. This effect persists more than twice as long as in *Mills et al.* [2008], which did not include any ocean cooling effects.

### 3.3. Global Mean Climate Anomalies

The global climate anomalies shown in Figure 3 respond very similarly in our 50 nm experiment ensemble and our 100 nm experiment; here we discuss the 50 nm calculations. The 3.6 Tg of BC that reaches the middle atmosphere and spreads globally absorbs the incoming SW solar radiation, reducing the net SW flux at the surface by ~12 W/m$^2$ initially or about 8% (Figure 3b). This anomaly tracks the evolution of the global mass burden of BC proportionally, similar to those calculated by GISS ModelE and SOCOL3. The SW flux in SOCOL3 seems to be more sensitive to BC than CESM1(WACCM), calculating comparable initial flux reductions with significantly lower BC burdens. In contrast, GISS ModelE and CESM1(WACCM) have similar sensitivity, producing very comparable flux anomalies in years 4 and 5, when the global mass burdens match most closely for the two models. After 10 years, our calculated SW flux anomaly persists at
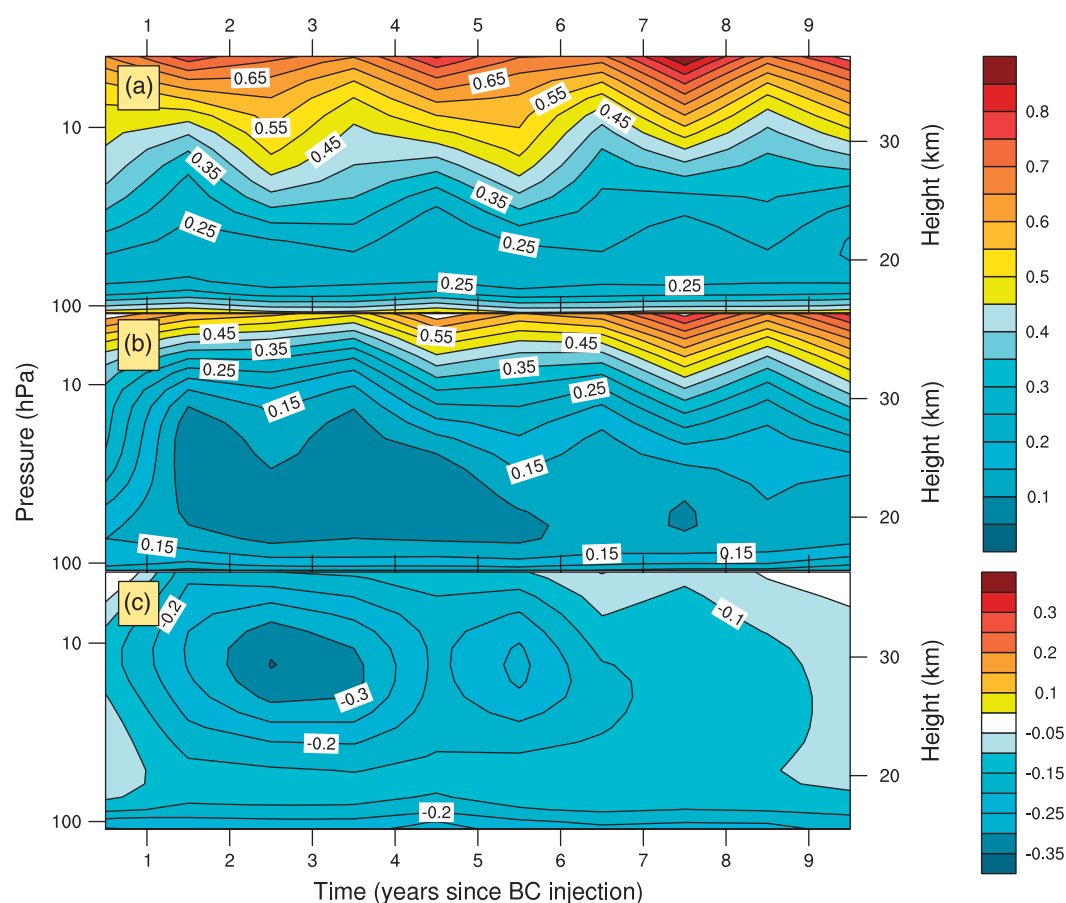
**Figure 4.** The time evolution of the tropical lower stratospheric vertical wind (mm/s) is shown for (a) the control, (b) the 50 nm experiment, and (c) and the experiment minus the control. Values are ensemble averages for latitudes 22°S to 22°N. The horizontal axis shows time in years. The left vertical axis shows pressure in hPa, and the right shows approximate pressure altitude in km.

−3.8 W/m², comparable to the maximum forcing of the 1991 Mount Pinatubo volcanic eruption [*Kirchner et al.*, 1999]. This is 2.7 times that of the flux anomaly calculated by GISS ModelE, with 2.0 times the mass burden. SOCOL3 fluxes have returned to normal after 10 years as BC mass burdens become insignificant. CESM1(WACCM) takes twice as long (20 years) to do the same.

Our calculated global average surface temperatures drop by ∼1.1 K in the first year (Figure 3c). This response is initially slower than that calculated by the GISS ModelE, due to the large initial rainout, but comparable to SOCOL3. The initial temperature anomalies for the three models correspond proportionately to their initial SW anomalies. Our temperatures continue to decrease for 5 years, however, reaching a maximum cooling of 1.6 K in year 5, 2–2.5 years after GISS ModelE and SOCOL3 begin warming from their maximum cooling of comparable magnitude. After a decade, our calculated global average cooling persists at ∼1.1 K, two to four times that calculated by GISS ModelE and SOCOL3. For CESM1(WACCM) and GISS Model E, this difference is roughly proportional with the ratio of mass burdens calculated. Our calculated cooling lags the recovery in mass burden and SW flux, however. Global average temperatures remain 0.25–0.50 K below the control ensemble average in years 20–23, after SW fluxes have returned to the control range. The thermal inertia of the oceans, which have experienced more than a decade of prolonged cooling, is responsible for much of this lag.

Precipitation rates drop globally by ∼0.18 mm/day within the first year after the conflict. This 6% loss in the global average persists for 5 years, during which time our calculated response is not as strong as that calculated by either GISS ModelE or SOCOL3. The fairly constant precipitation anomaly that we calculate over the first 5 years is explained by the opposing trends in surface temperature and SW flux over this period, which tend to cancel each other out. In year 5, however, precipitation drops further as

temperatures continue to fall, reaching a maximum reduction of 9% in global precipitation while precipitation in the other two models is in their second year of recovery. At the end of a decade, our calculated global precipitation is still reduced by 4.5%, and more than five times the reduction calculated at that time by GISS ModelE or SOCOL3. After 26 years, global average temperature and precipitation both remain slightly below the control ensemble average.

### 3.4. Ocean and Sea Ice Response

As Figure 5 shows, sea ice extent expands significantly over the first 5 years in the Arctic, and the first 10 years in the Antarctic. Sea ice extent is defined as the total area of all surface grid points in the ocean
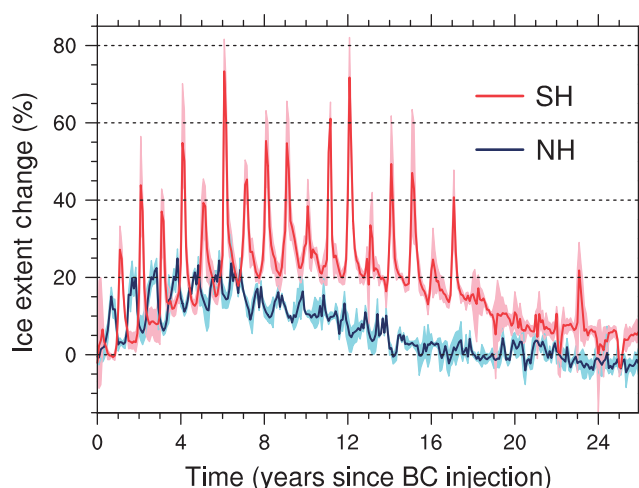


model with sea ice coverage greater than 15%. Both hemispheres experience an earlier onset of sea ice formation in the autumn, as revealed by the seasonal maxima, consistent with *Stenke et al.* [2013]. In the Arctic, sea ice extent increases peak at 10%–25% in years 4–7. Antarctic sea ice extent peaks at 20%–75% larger than the control ensemble in years 7–15, and remains 5%–10% larger throughout the years 20–26. These vast expansions of sea ice affect not only transfer of energy between the atmosphere and the oceans but also enhance planetary albedo, further cooling the surface by reflecting more sunlight to space. Expanding sea ice would also have large impacts on ocean life, strongly impacting the range of organisms that are in equilibrium with the current climate [e.g., *Harley et al.*, 2006].

**Figure 5.** Change in sea ice extent (%) for the 50 nm experiment is shown relative to the control. Sea ice extent is defined as the area of all sea surface grid points with ice fraction greater than 15%. The red line shows the ensemble average anomaly for the Southern Hemisphere. The blue line shows the same for the Northern Hemisphere. Shading around each line shows the range of the experiment ensemble runs with respect to the control ensemble average. The horizontal axis shows time in years. The vertical axis shows relative change in ice extent area, 100% × (experiment − control)/control.

We also find that the upper layer of the ocean experiences a prolonged cooling that penetrates to hundreds of meters depth. Figure 6 shows the monthly global average ocean temperature anomalies at various depths for the 50 nm experiment ensemble, including ensemble variability, compared to the control ensemble average. As the figure shows, average cooling exceeding 0.5 K extends to 100 m depth through year 12. The upper 2.5 m of the ocean has the same heat capacity per unit area as the whole depth of the atmosphere [*Gill*, 1982]. Hence, this significant cooling down to 100 m depth creates a long-lived thermal deficit that maintains reduced surface temperature for decades. The temperature response takes longer to penetrate to deeper waters, with temperatures at 1000 m continuing to drop for all 26 years simulated.

### 3.5. Stratospheric Ozone Loss

The absorbing BC not only cools the surface but also severely heats the middle atmosphere (Figure 7). As in *Mills et al.* [2008], we calculate initial global average temperature increases in excess of 80 K near the stratopause (50–60 km). As in *Robock et al.* [2007b], we calculate global average stratospheric heating in excess of 30 K for the first 5 years. Figure 7 also reveals the surface cooling discussed above, as well as a cooling of the atmosphere above the BC layer, consistent with *Robock et al.* [2007b].

As in *Mills et al.* [2008], we calculate massive ozone loss as a consequence of these extreme stratospheric temperatures (Figure 8). Consistent with that work, we calculate a global average column ozone loss of 20%–25% persisting from the second through the fifth year after the nuclear war, and recovering to 8% column loss at the end of 10 years. Throughout the first 5 years, column ozone is reduced by 30%–40% at midlatitudes and by 50%–60% at northern high latitudes.
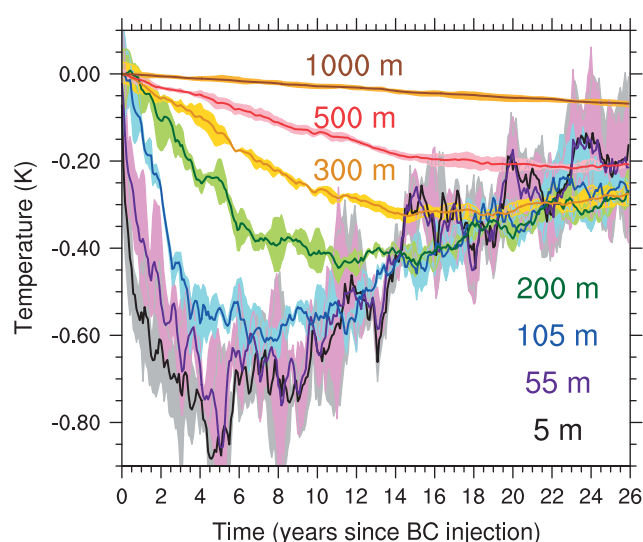
**Figure 6.** The time evolution of the global average ocean temperature anomaly at various depths is shown. The lines show the monthly average of the experiment ensemble temperatures minus the monthly average of the control ensemble. Shading around each line shows the range of the experiment ensemble runs with respect to the control ensemble average. The horizontal axis shows time in years. The vertical axis shows temperature in K.

As *Mills et al*. [2008] discussed, this ozone loss results primarily from two temperature-sensitive catalytic loss cycles involving odd oxygen and odd nitrogen, which accelerate at high temperatures. In addition, analysis of our current results shows that heating of the tropical tropopause allows up to 4.3 times as much water vapor to enter the lower stratosphere. The enhanced water vapor has a twofold effect on depleting ozone. Photolysis of water vapor produces both odd hydrogen and excited-state atomic oxygen, $O(^1D)$, depending on the wavelength of dissociating sunlight. $O(^1D)$ is responsible for the production of odd nitrogen in the stratosphere via reaction with $N_2O$. Odd hydrogen has its own catalytic cycle destroying ozone. We calculate that odd hydrogen in the tropical lower stratosphere is enhanced by factors of 3–5.5 over the first 2 years after
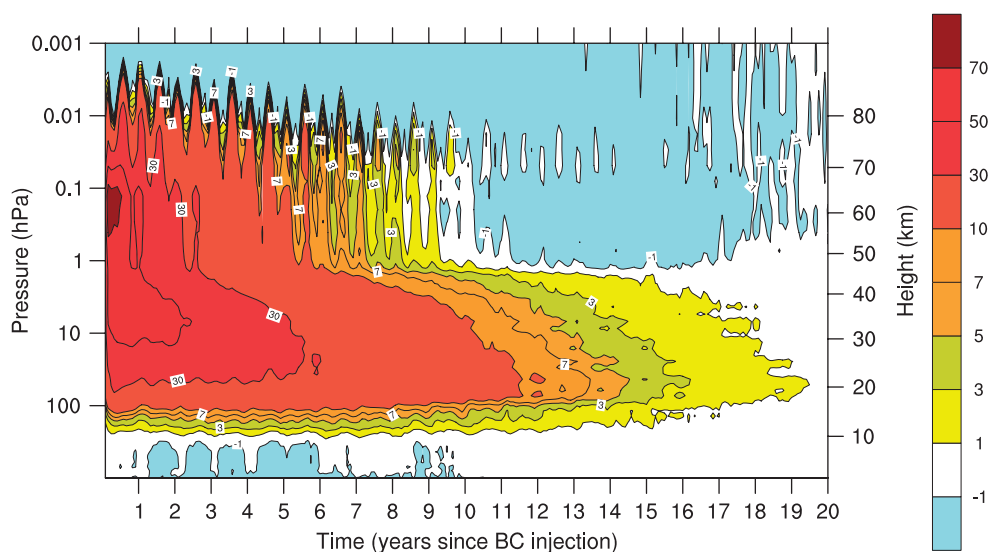
the nuclear war. Similarly, $O(^1D)$ is enhanced in the same region by factors of 4–7.6. $O(^1D)$ is not the major loss mechanism for $N_2O$ in the stratosphere, however, and $N_2O$ levels are initially slightly elevated in the tropical stratosphere, likely due to uplift by the initial rise of the plume, as described by *Mills et al*. [2008]. Subsequent slowing of the stratospheric circulation produces reduced $N_2O$ levels, as increased age of air results in increased chemical loss.

Ozone production rates are highest in the Tropics, where losses are dominated by transport of ozone to higher latitudes. As air is transported poleward, the chemical losses accumulate, leading to higher column losses at higher latitudes. At southern high latitudes, ozone losses are mitigated by the elimination



**Figure 7.** The time evolution of the vertical profile of global average temperature anomaly is shown. Values are for the 50 nm experiment ensemble average minus the control ensemble average. The horizontal axis shows time in years. The left vertical axis shows pressure in hPa, and the right vertical axis shows approximate pressure altitude in km. Contours show temperature anomalies in K.
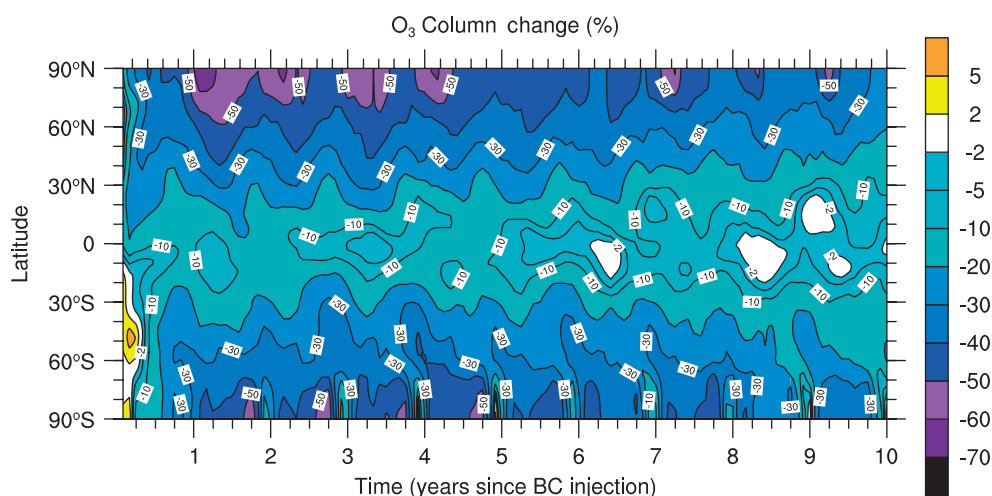
**Figure 8.** The time evolution of the change (%) in zonal mean column ozone is shown. The change in the 50 nm experiment ensemble average is shown relative to the control ensemble average: 100% × (experiment − control)/control. The horizontal axis shows time in years. The vertical axis shows latitude.

of the seasonal Antarctic ozone hole, which normally results from heterogeneous chemistry occurring on polar stratospheric clouds (PSCs) only at the extreme low temperatures present in the Antarctic stratosphere. We do not include effects of heterogeneous chemistry on BC aerosol, which is less understood than chemistry on sulfates and PSCs.

### 3.6. Changes in Surface UV Radiation

We used the TUV (tropospheric ultraviolet-visible) model [*Madronich and Flocke*, 1997] to calculate the impacts of this massive ozone loss on fluxes of damaging UV radiation reaching the Earth's surface. TUV simulates the attenuation of sunlight on its journey through Earth's atmosphere. The model has been used to study a wide range of topics including chemistry of the remote [*Walega et al.*, 1992] and urban atmosphere [*Castro et al.*, 2001], chemistry within snowpacks [*Fisher et al.*, 2005], incidence of skin cancer [*Thomas et al.*, 2007], methane emissions from plants [*Bloom et al.*, 2010], and potential changes to UV resulting from asteroid impacts [*Pierazzo et al.*, 2010] and geoengineering [*Tilmes et al.*, 2012]. The method used in this study is based on that described by *Lee-Taylor et al.* [2010].

We used TUV to calculate UV fluxes for clear sky conditions, based on the monthly average column ozone and absorbing BC distributions calculated for the control and experiment ensemble averages of our CESM1(WACCM) runs. To reduce computational overhead, we precalculated lookup tables of UV variation with respect to ozone, solar zenith angle ($\theta$), and surface elevation, using the full 80 km atmospheric column considered by TUV. We then constructed global distributions of UV from the modeled WACCM ozone distributions using Beer's law to account for the slant-path absorption by the stratospheric BC, performing the calculation daily to account for varying $\theta$. We express the monthly averaged UV results in terms of the international UV Index (UVI) [WHO, WMO, UNEP, and ICNIRP, 2002], which weights noontime UV fluxes by an "action spectrum" to account for the wavelength dependence of the effectiveness of solar radiation at causing skin damage [*McKinlay and Diffey*, 1987].

Figure 9 shows UVI in the peak summer months of June for the Northern Hemisphere and December for the Southern Hemisphere. The World Health Organization recommends that sun protection measures be taken for UV indices of 3 and above, and characterizes UVI values of 8–10 as "very high," warranting extra protection measures to avoid exposure to sunlight during midday hours. UVI greater than 11 is considered "extreme." We calculate UVI increases of 3–6 throughout the midlatitudes in summer, bringing peak values off the charts at 12–21 over the most populous regions of North America and southern Europe in June. We find similar increases for Australia, New Zealand, southern Africa, and South America in December. Skin damage varies with skin type, with burn times inversely proportional to UVI. Hence, a moderately fair-skinned North American who experiences a painful, noticeable sunburn after 10 min in the sun at noon in June for a UVI of 10 would receive an equivalent level of damage after 6.25 min for a UVI of 16.
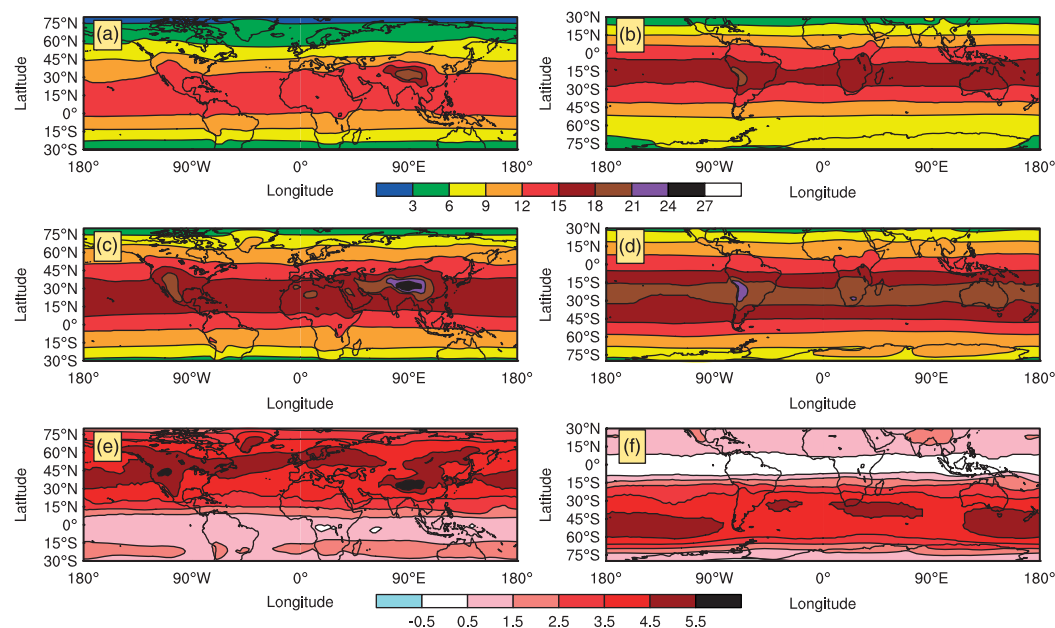
**Figure 9.** UV index in June (left) and December (right) is shown for the control (a, b), the experiment (c, d), and the experiment minus the control (e, f). Values are ensemble averages for year 3.

*Stenke et al.* [2013] calculate similarly dramatic increases in UV radiation due to ozone loss. They also report that the attenuation of solar fluxes from BC absorption was significant enough in high-latitude winter to reduce UV levels by 30% when they are most needed for vitamin D production. In contrast, we do not find that BC attenuation is significant enough to offset the UV increases from ozone loss.

The calculations shown in Figure 9 include absorption of UV by the BC, but not scattering, which presents an additional source of uncertainty. We performed a sensitivity test at 305 nm using a nominal single-scattering albedo of 0.31 for a 1 km depth soot layer centered on 27 km and a total ozone column of 200 DU. We calculate that BC scattering produces small reductions in ground-level UV irradiance, ranging from 4% for overhead sun and soot optical depth of 0.05 to 12% for $\theta$ of 88° and soot optical depth of 0.1. Hence, scattering would only marginally offset the 30%–100% increases in UV irradiance that we calculate for summer in the extratropics.

### 3.7. Effects on Vegetation and Agriculture

The severe increases in UV radiation following a regional nuclear war would occur in conjunction with the coldest average surface temperatures in the last 1000 years [*Mann et al.*, 1999]. Although global average surface temperatures would drop by 1.5 K (Figure 3c), broad, populated regions of continental landmasses would experience significantly larger cooling, as shown in Figure 10. Winters (JJA) in southern Africa and South America would be up to 2.5 K cooler on average for 5 years, compared to the same years (2–6) in the control run. Most of North America, Asia, Europe, and the Middle East would experience winters (DJF) that are 2.5–6 K cooler than the control ensemble, and summers (JJA) 1–4 K cooler.

Similarly, the 6% global average drop in precipitation that persists through years 2–6 (Figure 3d) translates into more significant regional drying (Figure 11). The most evident feature is over the Asian monsoon region, including the Middle East, the Indian subcontinent, and Southeast Asia. Broad precipitation reductions of 0.5–1.5 mm/day would reduce annual rainfall by 20%–80%. Similarly, large relative reductions in rainfall would occur in the Amazon region of South America, and southern Africa. The American Southwest and Western Australia would be 20%–60% drier. *Robock et al.* [2007b] predict a broadly wetter Sahel region as a result of a weaker Hadley circulation. *Stenke et al.* [2013] do not find such increased precipitation, and nor do we, despite some increase in precipitation near Morocco.

Following *Robock et al.* [2007b], we have calculated the change in the frost-free growing season, defined as the number of consecutive days in a 1 year period with minimum temperatures above 0°C (Figure 12).
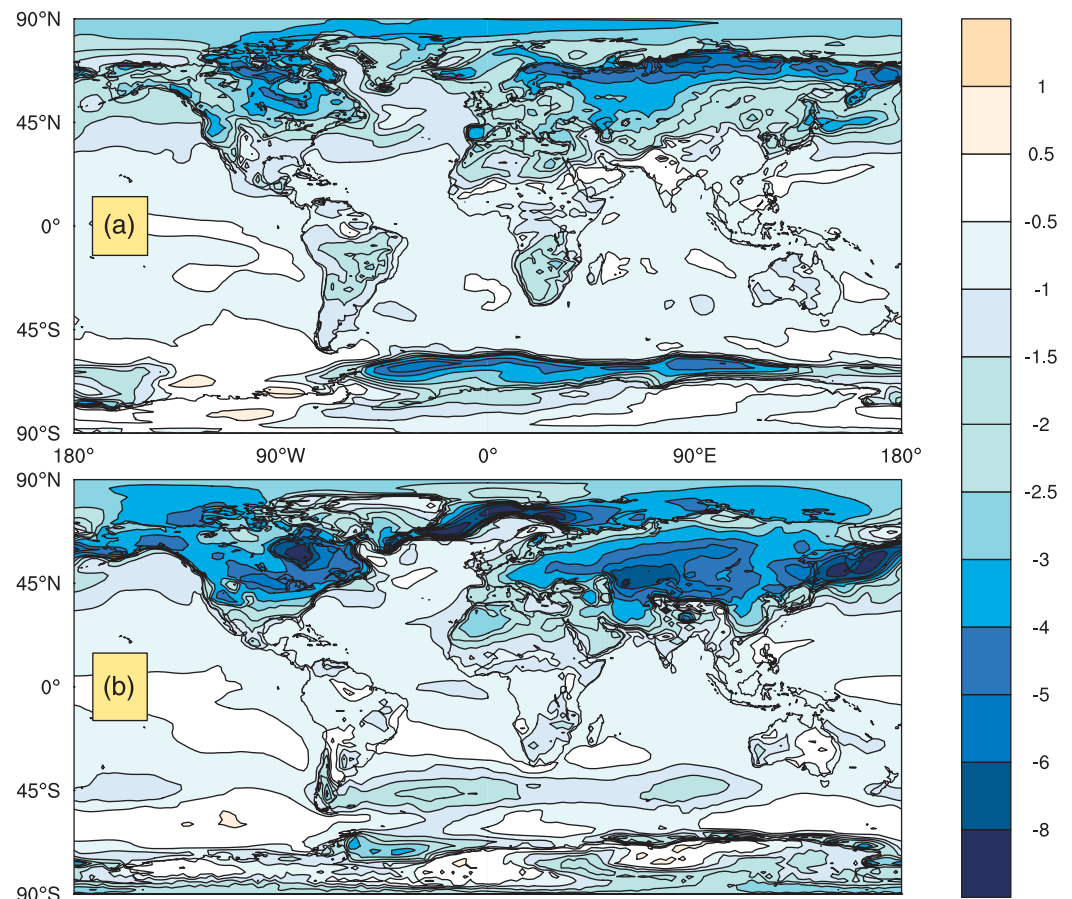
**Figure 10.** Change in surface temperature (K) for (a) June to August and (b) December to February. Values are 5 year seasonal ensemble averages for years 2–6, experiment minus control.

Because our globally averaged surface temperatures continue to cool until year 6, we show the average change in the growing season over years 2–6. The length of the average growing season is reduced by up to 40 days throughout the world's agricultural zones over these 5 years. This is similar to the results that *Robock et al.* [2007b] report for their first year, with significant regional differences. We find more significant decreases in Russia, North Africa, the Middle East, and the Himalayas than the previous study, and somewhat smaller effects in the American Midwest and South America.

The land component in CESM1(WACCM) is CLM4CN, a comprehensive land carbon cycle model [*Lawrence et al.*, 2011]. CLM4CN is prognostic with respect to carbon and nitrogen state variables in vegetation, litter, and soil organic matter. Vegetation carbon is affected by temperature, precipitation, solar radiation (and its partitioning into direct and diffuse radiation), humidity, soil moisture, and nitrogen availability, among other factors. We calculate an average loss of 11 Pg C from vegetation (2% of the total), which equates to an increase in atmospheric $CO_2$ of about 5 ppmv ($5 \times 10^{-6}$ molec/molec air). We also note a significant (42%–46%) increase in C loss from fires in the Amazon over the first 8 years in two of our three 50 nm experiment ensemble. The third run showed Amazon fire loss 13% higher than the control average, but within the variability of the control ensemble. Our runs do not account for the atmospheric effects of $CO_2$ or smoke emissions from the land component, but the smoke from the Amazon-kindled fires would be a positive feedback that would enhance the cooling we have found.

## 4. Discussion

*Pierazzo et al.* [2010] reviewed literature considering the effects of large and prolonged increases in UV-B radiation, similar to those we calculate, on living organisms, including agriculture and marine
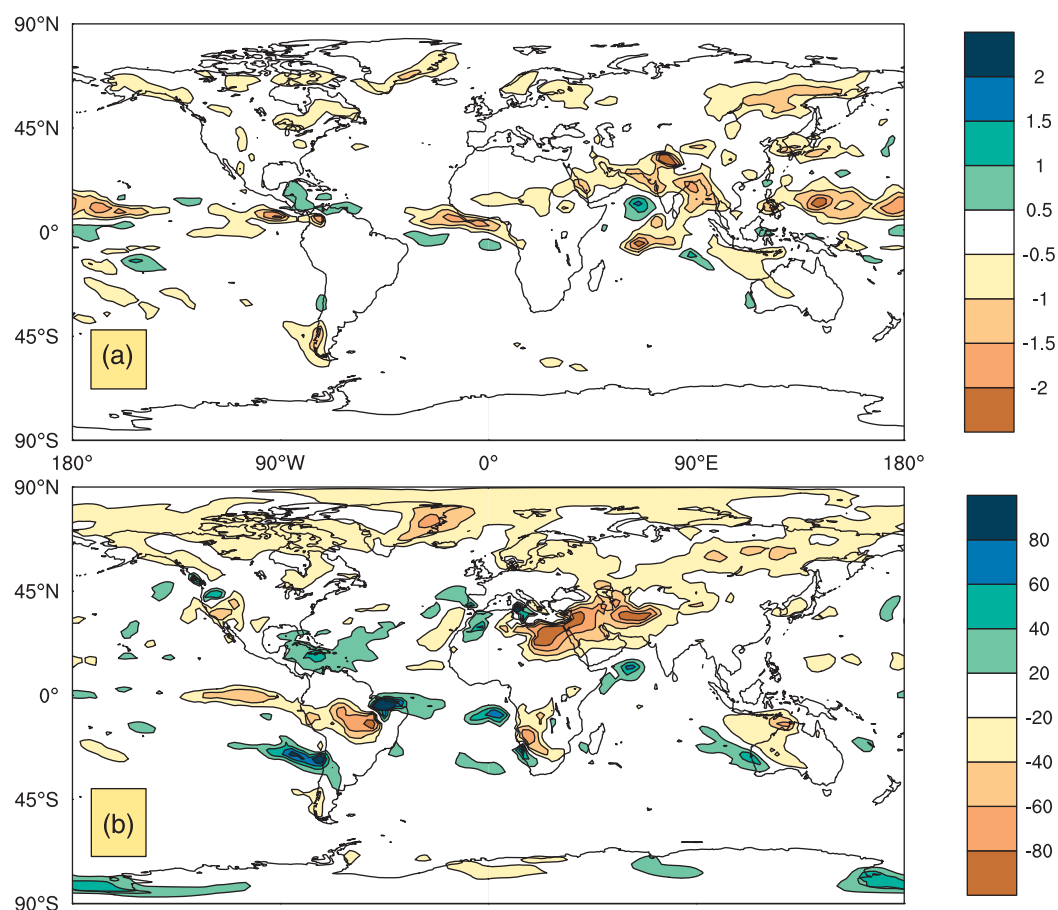
**Figure 11.** Changes in (a) absolute (mm/day) and (b) relative (%) surface precipitation. Values are 5 year seasonal ensemble averages for June to August, years 2–6, experiment minus control.
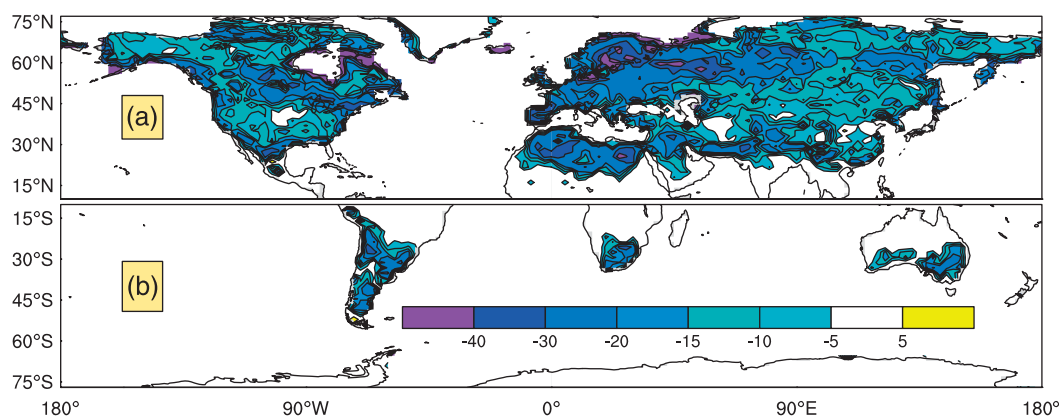


**Figure 12.** Change in frost-free growing season in days for (a) January to December in the Northern Hemisphere and (b) July to June in the Southern Hemisphere. Values are 5 year seasonal ensemble averages for years 2–6, experiment minus control.

ecosystems. General effects on terrestrial plants have been found to include reduced height, shoot mass, and foliage area [*Caldwell et al.*, 2007]. *Walbot* [1999] found the DNA damage to maize crops from 33% ozone depletion to accumulate proportionally to exposure time, being passed to successive generations, and destabilizing genetic lines. Research indicates that UV-B exposure may alter the susceptibility of plants to attack by insects, alter nutrient cycling in soils (including nitrogen fixation by cyanobacteria), and shift competitive balances among species [*Caldwell et al.*, 1998; *Solheim et al.*, 2002; *Mpoloka*, 2008].

The ozone depletion we calculate could also damage aquatic ecosystems, which supply more than 30% of the animal protein consumed by humans. *Häder et al*. [1995] estimate that 16% ozone depletion could reduce phytoplankton, the basis of the marine food chain, by 5%, resulting in a loss of 7 million tons of fish harvest per year. They also report that elevated UV levels damage the early developmental stages of fish, shrimp, crab, amphibians, and other animals. The combined effects of elevated UV levels alone on terrestrial agriculture and marine ecosystems could put significant pressures on global food security.

The ozone loss would persist for a decade at the same time that growing seasons would be reduced by killing frosts, and regional precipitation patterns would shift. The combination of years of killing frosts, reductions in needed precipitation, and prolonged enhancement of UV radiation, in addition to impacts on fisheries because of temperature and salinity changes, could exert significant pressures on food supplies across many regions of the globe. As the January to May 2008 global rice crisis demonstrated, even relatively small food price pressures can be amplified by political reactions, such as the fearful restrictions on food exports implemented by India and Vietnam, followed by Egypt, Pakistan, and Brazil, which produced severe shortages in the Philippines, Africa, and Latin America [Slayton, 2009]. It is conceivable that the global pressures on food supplies from a regional nuclear conflict could, directly or via ensuing panic, significantly degrade global food security or even produce a global nuclear famine.

## 5. Summary

We present the first simulations of the chemistry-climate effects of smoke produced by a nuclear war using an Earth system model that includes both stratospheric chemistry and feedbacks on sea ice and deep ocean circulation. We calculate impacts on surface climate persisting significantly longer than previous studies, as a result of several feedback mechanisms. First, BC absorbs sunlight, heating ambient air, and self-lofts to the upper stratosphere, a region treated with greater vertical resolution in CESM1(WACCM) than in the model used by *Robock et al*. [2007b]. Second, the BC spreads globally, absorbing sunlight, which heats the stratosphere and cools the surface. This has the effect of reducing the strength of the stratospheric circulation and increasing the lifetime of BC in the stratosphere. Third, the reduction of surface temperatures cools the upper 100 m of the ocean by >0.5 K for 12 years, and expands ice extent on sea and land. This lends inertia to the surface cooling due to both thermal mass and enhanced albedo, causing recovery in surface temperatures to lag the recovery in BC by a decade or more. As a result, we calculate that surface temperatures remain below the control ensemble range even 26 years after the nuclear war.

The global average temperature increase in the stratosphere following the BC injection initially exceeds 70 K, and persists above 30 K for 5 years, with full recovery taking two decades. As in previous studies, this temperature increase produces global ozone loss on a scale never observed, as a result of several chemical mechanisms. The resulting enhancements to UV radiation at the surface would be directly damaging to human health, and would damage agricultural crops, as well as ecosystems on land and in the oceans.

These results illustrate some of the severe negative consequences of the use of only 100 of the smallest nuclear weapons in modern megacities. Yet the United States, Russia, the United Kingdom, China, and France each have stockpiles of much larger nuclear weapons that dwarf the 100 examined here [*Robock et al*., 2007a; *Toon et al*., 2007]. Knowing the perils to human society and other forms of life on Earth of even small numbers of nuclear weapons, societies can better understand the urgent need to eliminate this danger worldwide.

## References

Bloom, A. A., J. Lee-Taylor, S. Madronich, D. J. Messenger, P. I. Palmer, D. S. Reay, and A. R. McLeod (2010), Global methane emission estimates from ultraviolet irradiation of terrestrial plant foliage, *New Phytol.*, 187(2), 417–425, doi:10.1111/j.1469-8137.2010.03259.x.

Caldwell, M. M., L. O. Björn, J. F. Bornman, S. D. Flint, G. Kulandaivelu, A. H. Teramura, and M. Tevini (1998), Effects of increased solar ultraviolet radiation on terrestrial ecosystems, *J. Photochem. Photobiol. B: Biol.*, 46(1), 40–52.

Caldwell, M. M., J. F. Bornman, C. L. Ballaré, S. D. Flint, and G. Kulandaivelu (2007), Terrestrial ecosystems, increased solar ultraviolet radiation, and interactions with other climate change factors, *Photochem. Photobiol. Sci.*, 6(3), 252–266, doi:10.1039/b700019g.

Castro, T., S. Madronich, S. Rivale, A. Muhlia, and B. Mar (2001), The influence of aerosols on photochemical smog in Mexico City, *Atmos. Environ.*, 35(10), 1765–1772, doi:10.1016/S1352-2310(00)00449-0.

Crutzen, P., and J. Birks (1982), Twilight at noon: The atmosphere after a nuclear war, *Ambio*, 11, 114–125.

Danabasoglu, G., S. C. Bates, B. P. Briegleb, S. R. Jayne, M. Jochum, W. G. Large, S. Peacock, and S. G. Yeager (2012), The CCSM4 ocean component, *J. Clim.*, 25(5), 1361–1389, doi:10.1175/JCLI-D-11-00091.1.

Fisher, F. N., M. D. King, and J. Lee-Taylor (2005), Extinction of UV-visible radiation in wet midlatitude (maritime) snow: Implications for increased NOx emission, *J. Geophys. Res.*, *110*(D21), D21301, doi:10.1029/2005JD005963.

Garcia, R. R., and W. J. Randel (2008), Acceleration of the Brewer-Dobson circulation due to increases in greenhouse gases, *J. Atmos. Sci.*, *65*(8), 2731–2739, doi:10.1175/2008JAS2712.1.

Gill, A. (1982), *Atmosphere-Ocean Dynamics*, Academic Press, San Diego, Calif.

Häder, D. P., R. C. Worrest, and H. D. Kumar (1995), Effects of increased solar ultraviolet radiation on aquatic ecosystems, *Ambio*, *24*, 174–180.

Harley, C. D. G., A. Randall Hughes, K. M. Hultgren, B. G. Miner, C. J. Sorte, C. S. Thornber, L. F. Rodriguez, L. Tomanek, and S. L. Williams (2006), The impacts of climate change in coastal marine systems, *Ecol. Lett.*, *9*, 228–241, doi:10.1111/j.1461-0248.2005.00871.x.

Hess, M., P. Koepke, and I. Schult (1998), Optical properties of aerosols and clouds: The software package OPAC, *Bull. Am. Meteorol. Soc.*, *79*, 831, doi:10.1175/1520-0477(1998)079<0831:OPOAAC>2.0.CO;2.

Holland, M. M., D. A. Bailey, B. P. Briegleb, B. Light, and E. Hunke (2012), Improved sea ice shortwave radiation physics in CCSM4: The impact of melt ponds and aerosols on Arctic sea ice, *J. Clim.*, *25*(5), 1413–1430, doi:10.1175/JCLI-D-11-00078.1.

Hurrell, J. W., et al. (2013), The community earth system model: A framework for collaborative research, *Bull. Am. Meteorol. Soc.*, *94*, 1339–1360, doi:10.1175/BAMS-D-12-00121.1.

Kinnison, D. E., et al. (2007), Sensitivity of chemical tracers to meteorological parameters in the MOZART-3 chemical transport model, *J. Geophys. Res.*, *112*, 20,302, doi:10.1029/2006JD007879.

Kirchner, I., G. L. Stenchikov, H.-F. Graf, A. Robock, and J. C. Antuña (1999), Climate model simulation of winter warming and summer cooling following the 1991 Mount Pinatubo volcanic eruption, *J. Geophys. Res.*, *104*(D), 19,039–19,056, doi:10.1029/1999JD900213.

Lawrence, D. M., et al. (2011), Parameterization improvements and functional and structural advances in Version 4 of the Community Land Model, *J. Adv. Model. Earth Syst.*, *3*(3), 45, doi:10.1029/2011MS000045.

Lee-Taylor, J., S. Madronich, B. Mayer, and C. Fischer (2010), A climatology of UV radiation, 1979–2000, 65S - 65N, in *UV Radiation in Global Climate Change: Measurements, Modeling and Effects on Ecosystems*, edited by W. Gao, D. Schmoldt, and J. Slusser, pp. 2–20, Springer, Heidelberg, Germany.

Madronich, S., and S. Flocke (1997), Theoretical estimation of biologically effective UV radiation at the Earth's surface, in *Solar Ultraviolet Radiation — Modeling, Measurements and Effects*, NATO ASI Ser., vol. I52, edited by C. Zerefos, pp. 23–48, Springer, Berlin, Germany.

Mann, M. E., R. S. Bradley, and M. K. Hughes (1999), Northern hemisphere temperatures during the past millennium: Inferences, uncertainties, and limitations, *Geophys. Res. Lett.*, *26*(6), 759–762, doi:10.1029/1999GL900070.

Marsh, D. R., M. J. Mills, D. E. Kinnison, J.-F. Lamarque, N. Calvo, and L. M. Polvani (2013), Climate change from 1850 to 2005 simulated in CESM1(WACCM), *J. Clim.*, *26*, 7372–7390, doi:10.1175/JCLI-D-12-00558.1.

McKinlay, F. A., and B. L. Diffey (1987), A reference action spectrum for ultraviolet induced erythema in human skin, in *Human Exposure to Ultraviolet Radiation*, edited by F. W. Passchier and B. Bosnjakovic, pp. 83–87, Elsevier, Amsterdam, Netherlands.

Meinshausen, M., et al. (2011), The RCP greenhouse gas concentrations and their extensions from 1765 to 2300, *Clim. Change*, *109*(1–2), 213–241, doi:10.1007/s10584-011-0156-z.

Mills, M. J., O. B. Toon, R. P. Turco, D. E. Kinnison, and R. R. Garcia (2008), Massive global ozone loss predicted following regional nuclear conflict, *Proc. Natl. Acad. Sci. U.S.A.*, *105*, 5307–5312, doi:10.1073/pnas.0710058105.

Mpoloka, S. W. (2008), Effects of prolonged UV-B exposure in plants, *Afr. J. Biotechnol.*, *7*(25), 4874–4883, http://www.ajol.info/index.php/ajb/article/viewFile/59692/47971.

National Research Council (1985), *The Effects on the Atmosphere of a Major Nuclear Exchange*, National Academy Press, Washington, D. C.

Neale, R. B., J. H. Richter, S. Park, P. H. Lauritzen, S. J. Vavrus, P. J. Rasch, and M. Zhang (2013), The mean climate of the community atmosphere model (CAM4) in forced SST and fully coupled experiments, *J. Clim.*, *26*, 5150–5168, doi:10.1175/JCLI-D-12-00236.1.

Oman, L., A. Robock, G. L. Stenchikov, T. Thordarson, D. Koch, D. T. Shindell, and C. Gao (2006), Modeling the distribution of the volcanic aerosol cloud from the 1783–1784 Laki eruption, *J. Geophys. Res.*, *111*, D12209, doi:10.1029/2005JD006899.

Pierazzo, E., R. R. Garcia, D. E. Kinnison, D. R. Marsh, and P. J. Crutzen (2010), Ozone perturbation from medium-size asteroid impacts in the ocean, *Earth Planet. Sci. Lett.*, *299*, 263–272, doi:10.1016/j.epsl.2010.08.036.

Pittock, A. B., T. Ackerman, P. Crutzen, M. MacCracken, C. Shapiro, and R. Turco (1985), *The Environmental Consequences of Nuclear War, vol. 1, Physical and Atmospheric Effects, SCOPE*, vol. 28, pp. 359, John Wiley, Chichester, U. K.

Robock, A., L. Oman, and G. L. Stenchikov (2007a), Nuclear winter revisited with a modern climate model and current nuclear arsenals: Still catastrophic consequences, *J. Geophys. Res.*, *112*, D13107, doi:10.1029/2006JD008235.

Robock, A., L. Oman, G. L. Stenchikov, O. B. Toon, C. G. Bardeen, and R. P. Turco (2007b), Climatic consequences of regional nuclear conflicts, *Atmos. Chem. Phys.*, *7*, 2003–2012, doi:10.5194/acp-7-2003-2007.

Ross, M., M. J. Mills, and D. Toohey (2010), Potential climate impact of black carbon emitted by rockets, *Geophys. Res. Lett.*, *37*(24), L24810, doi:10.1029/2010GL044548.

Slayton, T. (2009), Rice crisis forensics: How Asian governments carelessly set the world rice market on fire, Center for Global Development Working Paper No. 163., http://www.cgdev.org/sites/default/files/1421260_file_Slayton_Rice_Crisis_Forensics_FINAL.pdf.

Solheim, B., U. Johanson, T. Callaghan, J. Lee, D. Gwynn-Jones, and L. Björn (2002), The nitrogen fixation potential of arctic cryptogam species is influenced by enhanced UV-B radiation, *Oecologia*, *133*(1), 90–93, doi:10.1007/s00442-002-0963-z.

Stenke, A., C. R. Hoyle, B. Luo, E. Rozanov, J. Gröbner, L. Maag, S. Brönnimann, and T. Peter (2013), Climate and chemistry effects of a regional scale nuclear conflict, *Atmos. Chem. Phys.*, *13*, 9713–9729, doi:10.5194/acp-13-9713-2013.

Stephens, S., and J. Birks (1985), After nuclear war: Perturbations in atmospheric chemistry, *BioScience*, *35*(9), 557–562.

Thomas, N. E., et al. (2007), Number of nevi and early-life ambient UV exposure are associated with BRAF-mutant melanoma, *Cancer Epidemiol. Biomarkers Prev.*, *16*(5), 991–997, doi:10.1158/1055-9965.EPI-06-1038.

Tilmes, S., D. E. Kinnison, R. R. Garcia, R. Salawitch, T. Canty, J. Lee-Taylor, S. Madronich, and K. Chance (2012), Impact of very short-lived halogens on stratospheric ozone abundance and UV radiation in a geo-engineered atmosphere, *Atmos. Chem. Phys.*, *12*(2), 10,945–10,955, doi:10.5194/acp-12-10945-2012.

Toon, O. B., R. P. Turco, P. Hamill, C. S. Kiang, and R. C. Whitten (1979), A one-dimensional model describing aerosol formation and evolution in the stratosphere: II. Sensitivity studies and comparison with observations, *J. Atmos. Sci.*, *36*, 718–736, doi:10.1175/1520-0469(1979)036<0718:AODMDA>2.0.CO;2.

Toon, O. B., R. P. Turco, D. Westphal, R. Malone, and M. S. Liu (1988), A multidimensional model for aerosols: Description of computational analogs, *J. Atmos. Sci.*, *45*, 2123–2143, doi:10.1175/1520-0469(1988)0452.0.CO;2.

Toon, O. B., R. P. Turco, A. Robock, C. G. Bardeen, L. Oman, and G. L. Stenchikov (2007), Atmospheric effects and societal consequences of regional scale nuclear conflicts and acts of individual nuclear terrorism, *Atmos. Chem. Phys.*, *7*, 1973–2002, doi:10.5194/acp-7-1973-2007.

Toon, O. B., A. Robock, and R. P. Turco (2008), Environmental consequences of nuclear war, *Phys. Today*, *61*(12), 37–42, doi:10.1063/1.3047679.

Turco, R. P., P. Hamill, O. B. Toon, R. C. Whitten, and C. S. Kiang (1979), A one-dimensional model describing aerosol formation and evolution in the stratosphere: I. Physical processes and mathematical analogs, *J. Atmos. Sci.*, *36*, 699, doi:10.1175/1520-0469(1979)0362.0.CO;2.

Turco, R. P., O. B. Toon, T. P. Ackerman, J. B. Pollack, and C. Sagan (1983), Nuclear winter: Global consequences of multiple nuclear explosions, *Science*, *222*(4), 1283–1292, doi:10.1126/science.222.4630.1283.

Walbot, V. V. (1999), UV-B damage amplified by transposons in maize, *Nature*, *397*(6718), 398–399, doi:10.1038/17043.

Walega, J. G., B. A. Ridley, S. Madronich, F. E. Grahek, J. D. Shetter, T. D. Sauvain, C. J. Hahn, J. T. Merill, B. A. Bodhaine, and E. Robinson (1992), Observations of peroxyacetyl nitrate, peroxypropionyl nitrate, methyl nitrate and ozone during the Mauna Loa Observatory Photochemistry Experiment, *J. Geophys. Res.*, *97*, 10,311, doi:10.1029/91JD02288.

WHO, WMO, UNEP, and ICNIRP (2002), *Global Solar UV Index: A Practical Guide*, WHO, Geneva, Switzerland.